Supplementary Information for

Ultrafast and Steady-State Optical Characterization of Multilayer PdS_2

Vedran Brusar,[a,b] Ana Senkić,[a,c] Petra Ivatović,[b] Jordi Sancho-Parramon,[d] Patrick Seleš,[a] Jisheng Zhang,[e] Yanfen Wan,[e] Peng Yang,[e] Nataša Vujičić [a] and Silvije Vdović *[a]

[a]Center for Advanced Laser Techniques, Institute of Physics, Bijenička 46, 10000 Zagreb, Croatia. E-mail: silvije@ifs.hr

[b]Department of Physics, Faculty of Science, University of Zagreb, 10000 Zagreb, Croatia

[c]Institute of Physics, University of Münster, Wilhelm Klemm str. 10, 48149, Münster, Germany

[d]Ruđer Bošković Institute, Bijenička cesta 54, 10000 Zagreb, Croatia

[e]National Center for International Joint Research of Photoelectric Energy Materials and Application, School of Materials and Energy, Yunnan University, Kunming 650091, P. R. China

Atomic force microscopy

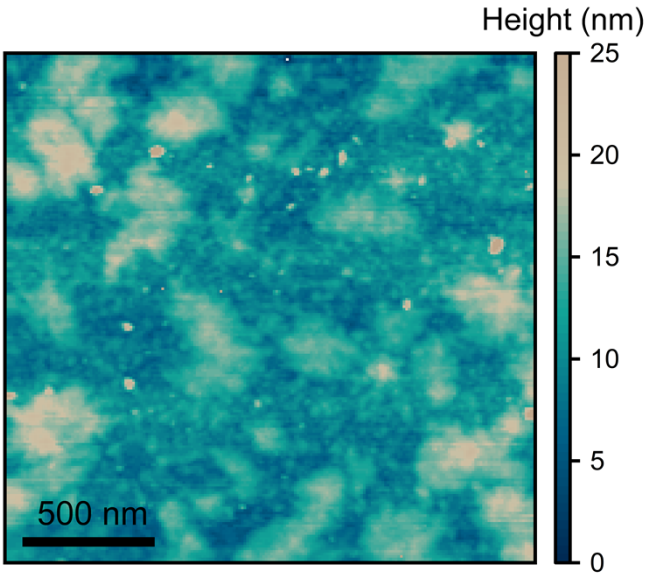

Fig. S1 Zoomed-in image of PdS_2 morphology showing sub-micron higher islands on the substrate.

Spectroscopic ellipsometry

Dispersion model used for representing the optical constants of PdS_2:

The real (ε_R) and imaginary (ε_I) part of the dielectric function as a function of the photon energy (E) for the PdS_2 layer are modelled as follows:

$$\varepsilon_R(E) = 1 + \frac{A_p}{E_p^2 - E^2} + \frac{2}{\pi} P \int_0^\infty \frac{\mu\, \varepsilon_I(\mu)}{\mu^2 - E^2} d\mu, \tag{S1}$$

$$\varepsilon_I(E) = A_{g1}\left(e^{-\left(\frac{E - E_{g1}}{\sigma_{g1}}\right)^2} - e^{-\left(\frac{E + E_{g1}}{\sigma_{g1}}\right)^2}\right) + A_{g2}\left(e^{-\left(\frac{E - E_{g2}}{\sigma_{g2}}\right)^2} - e^{-\left(\frac{E + E_{g2}}{\sigma_{g2}}\right)^2}\right). \tag{S2}$$

The second term in ε_R accounts for the pole contribution characterized by its strength A_p and energy E_p while the third term is the contribution of the interband transitions calculated via Kramers-Kronig relation where P denotes the Cauchy principal value. The interband transitions are described by two Gaussian oscillators contribution to $\varepsilon_I(E)$, each one described by three parameters: amplitude (A_g), position (E_g) and braodening (σ_g).

model (MSE 5.25):

Optimal thickness and dispersion parameter values obtained by best fitting the experimental data.

Thickness: 7.56 ± 0.12 nm

A_p: 75 ± 6

E_p: 6.3 ± 0.2 eV

Table S1 Results of the fitting procedure from ellipsometric measurement.

	A_g	E_g (eV)	σ_g (eV)
Oscillator 1	8.7±0.2	2.203±0.003	0.77±0.01
Oscillator 2	9.2±0.2	3.63±0.04	2.85±0.05

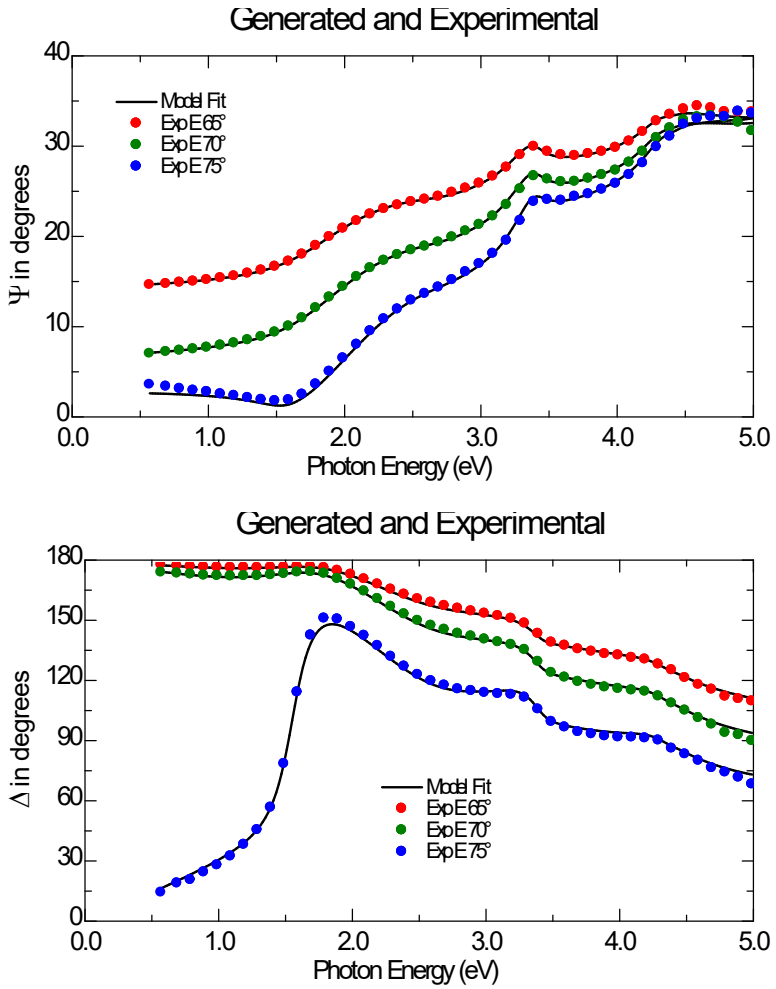

Fig. S2 Experimental ellipsometric data (symbols) as a function of photon energy and angle of incidence, together with the corresponding best fits (solid lines) for the PdS_2 sample.

Critical-point analysis:

The second derivative of the dielectric function was simultaneously fitted for both the real and imaginary parts using the following expression:

$$\frac{d^2\varepsilon}{dE^2} = \mathrm{A}e^{i\phi}(E - E_t - i\Gamma)^{n-2} \tag{S3}$$

Table S2 Results of the critical-point fitting procedure.

n	A	Φ (rad)	E_t (eV)	Γ (eV)	R^2
0.5 (3D)	5.6 ± 0.3	0.30 ± 0.09	2.11 ± 0.02	0.26 ± 0.01	0.8257
0 (2D)	5.7 ± 0.3	1.0 ± 0.4	2.10 ± 0.04	0.37 ± 0.04	0.8930
-1 (exciton)	8.1 ± 0.3	2.56 ± 0.05	2.08 ± 0.01	0.597 ± 0.008	0.9541

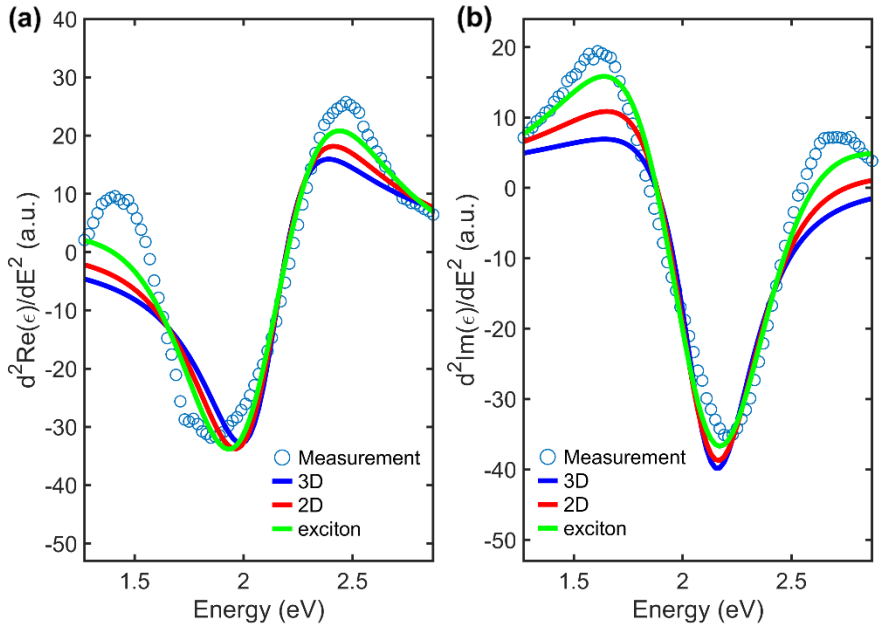

Fig. S3 Second derivatives of the real part (a) and the imaginary part (b) of the dielectric function, and the fitted lineshapes predicted by critical-point model.

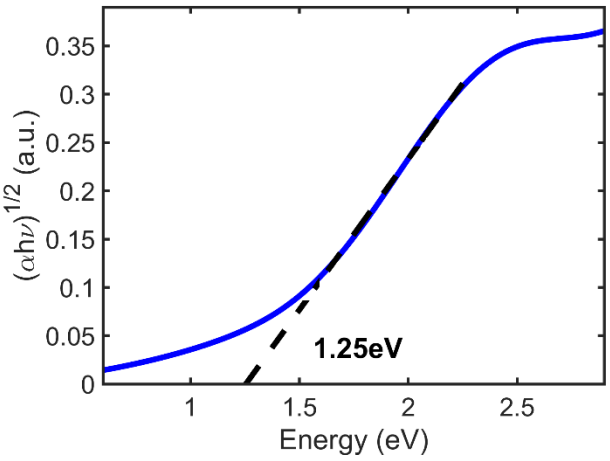

Fig. S4 Tauc plot derived from the absorption coefficient of PdS_2 with an indirect optical transition at 1.25 eV.

Raman spectroscopy

Table S3 Results of the fitting procedure of multilayer PdS_2 Raman spectrum on sum of multiple Lorentzian functions.

Assignation	Frequency (cm^{-1})	FWHM (cm^{-1})	Intensity (a.u.)
A	158.4 ± 0.3	4.2 ± 0.7	2700 ± 300
$A_g^1 + B_{1g}^1$	245.44 ± 0.06	6.6 ± 0.2	23300 ± 400
A_g^2	362.3 ± 0.5	4 ± 1	1300 ± 400
B_{1g}^2	384.8 ± 0.1	6.3 ± 0.4	9400 ± 400
A_g^3	464.70 ± 0.04	7.1 ± 0.1	37500 ± 500
B_{1g}^3	482.3 ± 0.2	4.8 ± 0.7	3300 ± 400

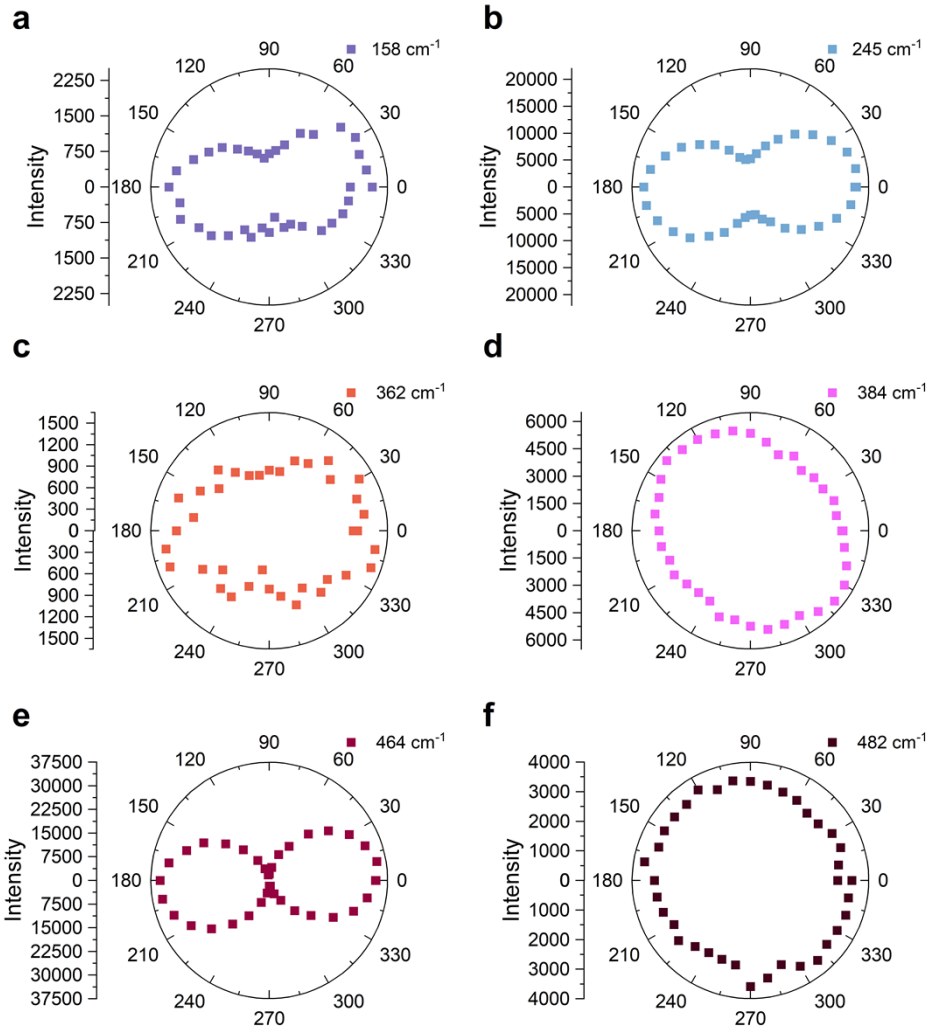

Fig. S5 Polarization dependent intensity of vibrational modes in multilayer PdS_2.

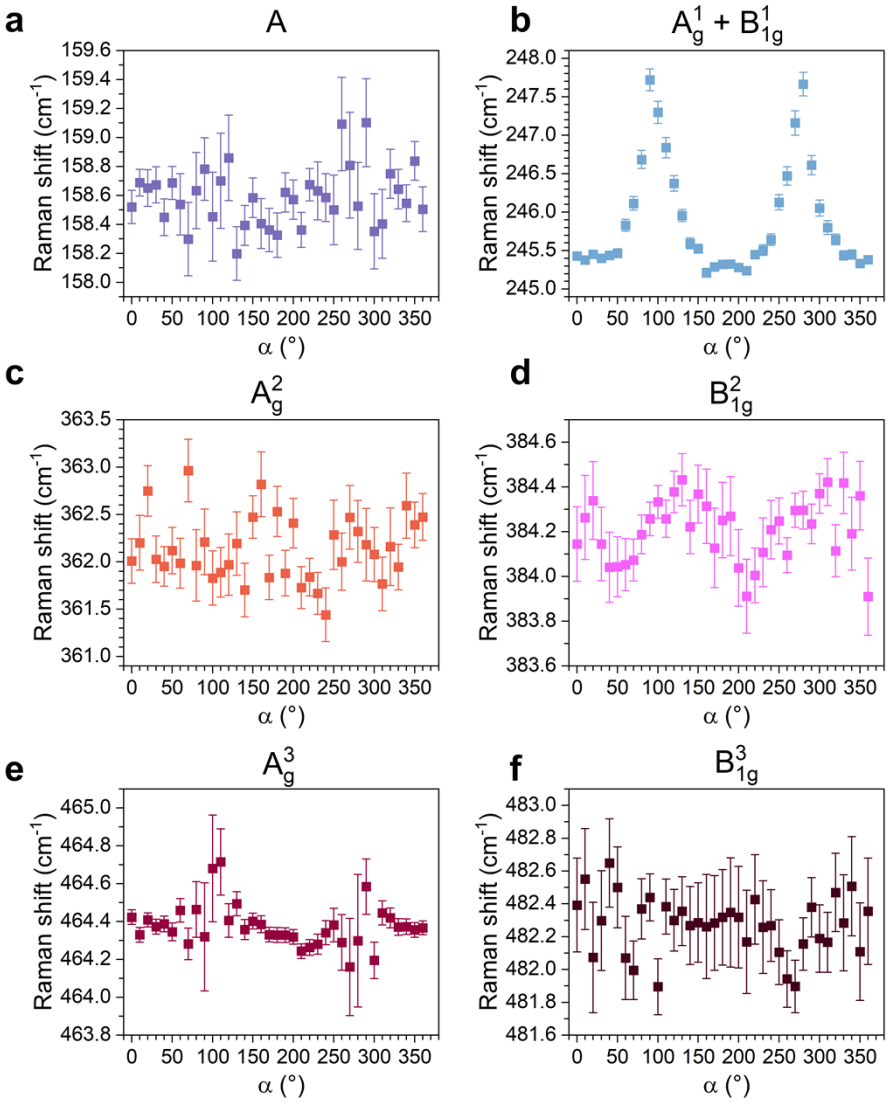

Fig. S6 Polarization dependent frequency of vibrational modes in multilayer PdS_2.

PdS_2 phases and Raman misassignment

Beyond the orthorhombic (2O) phase, PdS_2 exhibits several other polymorphs. These include a high-pressure pyrite (2C) phase, stabilized above ≈16 GPa, and reported to become superconducting with a critical temperature of 8 K at 37.4 GPa,[S1] as well as a so-far purely theoretical CdI_2-type (1T) phase. Among all proposed structures, the 2O phase is predicted to be the thermodynamic ground state for all thicknesses. Its enhanced stability has been attributed to the formation of chalcogen dimers, and methods such as laser irradiation or electrostatic doping have been proposed as possible routes for inducing a 2O → 1T transition.[S2]

For the 1T- PdS_2, recent calculations predict band gaps of 0.54 eV in bulk and 1.7 eV in the monolayer limit.[S2] These values are significantly larger than those obtained from conventional PBE-based DFT calculations and do not support the previously proposed semimetal-to-semiconductor transition. Consequently, several applications predicted based on such a transition,[S3] would not be feasible in PdS_2, although they may remain viable in the related compound 1T-$PdSe_2$, where the transition is theoretically supported. The same study predicts only two Raman-active modes for 1T-PdS_2, namely the E_g and A_{1g} modes, in bulk at approximately 315 cm^{-1} and 340 cm^{-1}, and at approximately 306 cm^{-1} and 337 cm^{-1} in the monolayer, respectively.[S2]

Silicon, as noted in the main text, exhibits a strong first-order Raman peak at 520 cm^{-1}, corresponding to scattering from the zone-center transverse optical (TO) phonons, as well as a prominent second-order feature near 300 cm^{-1} arising from two transverse acoustic (TA) phonons near the X point of the Brillouin zone.[S4,S5] In addition, present on the same broad second-order feature extending 220 to 460 cm^{-1}, a peak at around 430 cm^{-1}, as well as the termination of scattering at around 460 cm^{-1} are often observed, which have been attributed to scattering involving phonons along and near the Σ point of the Brillouin zone.[S4] Furthermore, Raman features of thin amorphous silicon oxide also lie in the same energy range and modulates the intensity depending on its thickness. A Raman spectrum measured on our bare Si/SiO_2 substrate is shown in Fig. S7 and is consistent with previous reports.[S4–S9]

In several reports,[S10–S13] Raman features near 300 cm^{-1} and 420 cm^{-1} were assigned to the E_g and A_g modes (or sometimes A_g^1 and A_g^2 overlapping) of PdS_2. Such an assignment would imply the presence of the 1T phase or maybe 2C, which, as discussed above, are not expected to form under standard synthesis conditions. More importantly, the reported peak positions disagree with theoretical predictions for Raman-active modes in any known PdS_2 polymorph. Furthermore, the linewidths, low intensities, and spectral shapes of the observed peaks—possibly often further distorted by background subtraction procedures—are more like those of second-order silicon scattering, rather than Raman modes of any PdS_2 phase. Since all reported measurements were performed on silicon substrates, a straightforward and reasonable explanation could be that these features originate from the substrate and were inadvertently misassigned to PdS_2.

This misinterpretation appears to have propagated further in the literature. In one case,[S12] a well-defined Raman response characteristic of orthorhombic PdS_2 was instead attributed to PdS_3, a phase that has neither been independently confirmed nor reported elsewhere.

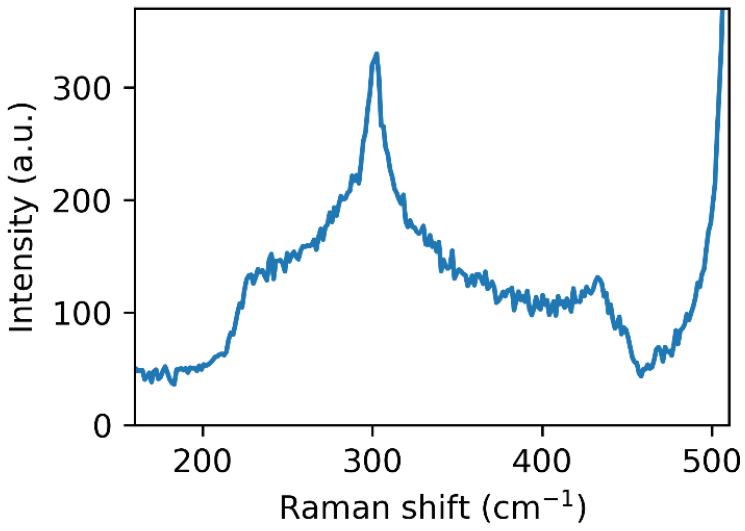

Fig. S7 Raman spectrum of bare Si/SiO_2 substrate.

Differential reflectance

Global analysis:

The three-compartment sequential model captures the temporal evolution of the PdS_2 transient spectra. The extracted Evolution Associated Spectra (EAS) in Fig. S8 reveal a progressive blue-shift of the response, consistent with hot-carrier cooling and bandgap renormalization recovery. The final, long-lived component exhibits a nearly constant spectral profile and is associated with the cold-carrier population. We also applied the same three-compartment sequential model to measurements with different pump fluences. The resulting fits show qualitatively similar behavior, again resolving a sub-picosecond and a picosecond component in the early-time response, as shown in Fig. S9. No clear systematic fluence dependence of the extracted early-time time constants can be established from these results. The lowest-fluence dataset (0.24 mJ/cm^2) is not shown because its transient signal had insufficient signal-to-noise ratio for reliable global fitting.

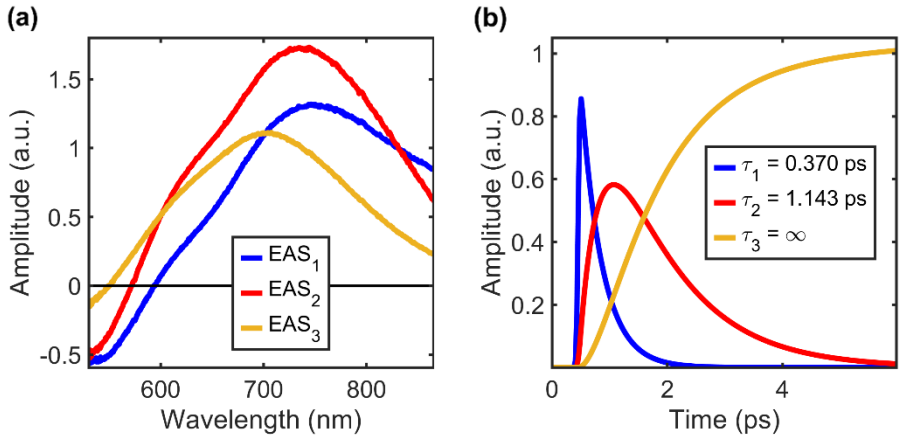

Fig. S8 Global analysis results using three-compartment sequential model at a pump fluence of 1.3 mJ/cm^2. (a) Evolution Associated Spectra (EAS), and (b) time profiles of the EAS spectra with corresponding decay constants shown in legend.

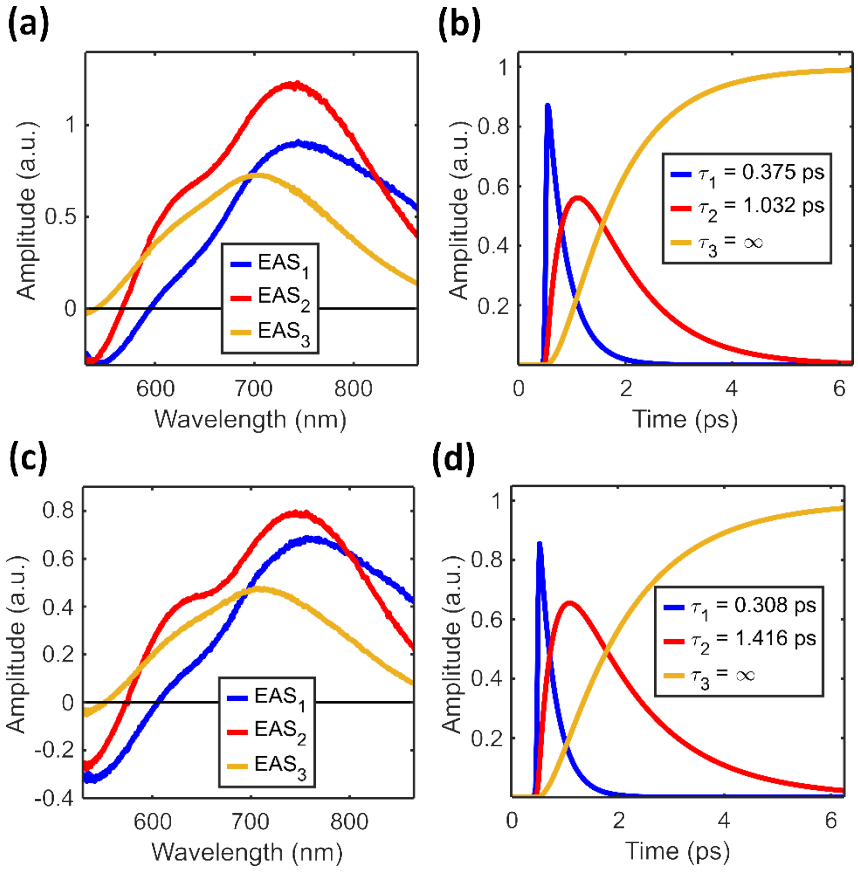

Fig. S9 Global analysis results using the three-compartment sequential model for two additional pump fluences. Panels (a) and (c) show the Evolution Associated Spectra (EAS), while panels (b) and (d) present the corresponding EAS temporal profiles with decay constants indicated in the legends. The pump fluences are 0.85 mJ/cm^2 for panels (a,b) and 0.59 mJ/cm^2 for panels (c,d).

Qualitative model of the transient spectral response:

A simple model calculation was performed to test whether the broad positive transient signal can arise from a modification of the equilibrium optical response. Starting from the dielectric function obtained from ellipsometry, the equilibrium dielectric response was shifted and the corresponding real part was recalculated from the shifted imaginary part using the Kramers–Kronig relation. The optical response of the air/PdS_2/SiO_2/Si structure was then evaluated within a transfer-matrix formalism[S14] using the ellipsometrically determined layer thicknesses. The resulting changes in absorption and reflectance reproduce the transient signal qualitatively. The model therefore supports the view that pump-induced modification of the equilibrium optical transition contributes to the positive transient response. Owing to overlapping photoinduced contributions and the sensitivity of the calculated spectral position to interference effects and effective film thickness, the analysis is used here only as a qualitative illustration. Since the model is simple, small differences between the calculated and measured spectra are expected. These differences may arise from photoinduced effects not included in the model, such as state filling and bleaching, linewidth broadening, changes in oscillator strength, and interference effects related to the nonuniform multilayer film.

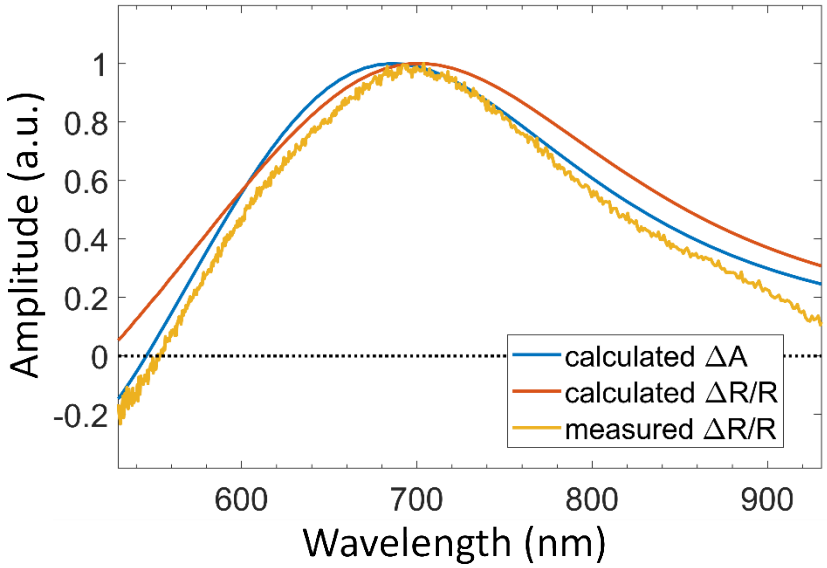

Fig. S10 Calculated ΔA and ΔR/R, obtained by shifting the imaginary part of the equilibrium dielectric function by 100 meV, together with the corresponding measured spectrum at 2 ps. The calculation used layer thicknesses of 7.56 nm for PdS_2 and 4.64 nm for SiO_2.

Single-wavelength fitting:

To characterize the dynamics beyond the initial few picoseconds, we performed single-wavelength fitting of the DR time traces across the spectral range of the positive DR signal. The fits were performed using a biexponential decay model, and the extracted decay constants are summarized in Fig. S11. The average values of decay constants obtained from the single-wavelength fits are reported in the main text. For the long-time dynamics, the first 50 ps were omitted from the fitting procedure due to a small rising signal that is attributed to the substrate contribution. Since multilayer PdS_2 is grown on a Si substrate, the pump pulse can excite the underlying Si layer, which in turn can modify the measured DR signal.[S15] As seen in Fig. S11d, silicon's photoinduced reflectivity change in wavelength range of the probe is negative and decays monotonically. In the PdS_2 signal, we observe a slow rise between ~10 and 30 ps, which coincides with the Si decay, as demonstrated by the overlapping curves shown in the inset of Fig. S11d. We therefore attribute this slow rise in the PdS_2 signal to the contribution from the photoexcited Si substrate.

To test whether the long-lived relaxation depends on excitation density, we repeated the same single-wavelength biexponential fitting procedure for different pump fluences. Representative fits and the extracted fitting parameters are shown in Fig. S12. Within experimental uncertainty, the extracted decay constants do not show significant fluence dependence over the investigated range.

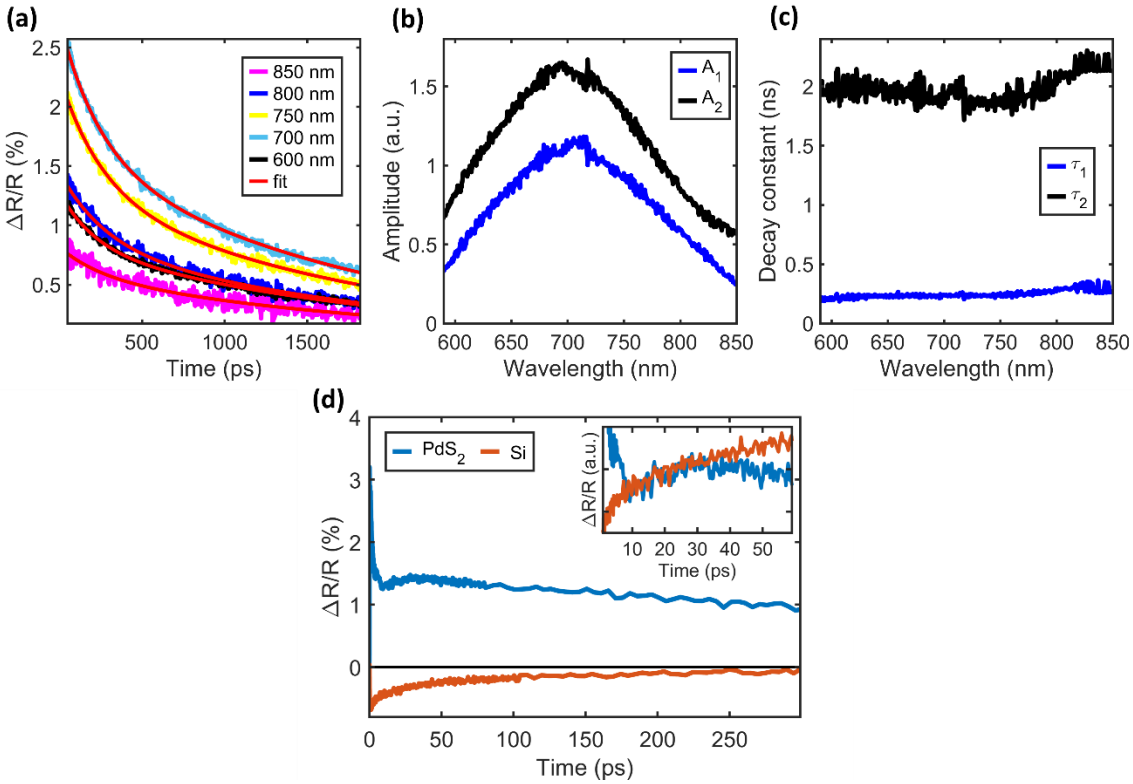

Fig. S11 Single wavelength fitting results of the longer-times dynamics using biexponential function at a pump fluence of 1.3 mJ/cm^2. (a) Selected DR time traces and corresponding fit curves. (b) Amplitude parameters dependence on probe wavelength. (c) Decay constant parameter dependence on probe wavelength. (d) Transient response of PdS_2 and the bare Si substrate measured at a probe wavelength of 800 nm. Inset: the curves are overlapped to illustrate the correspondence, with a vertical offset applied to one trace for clarity.

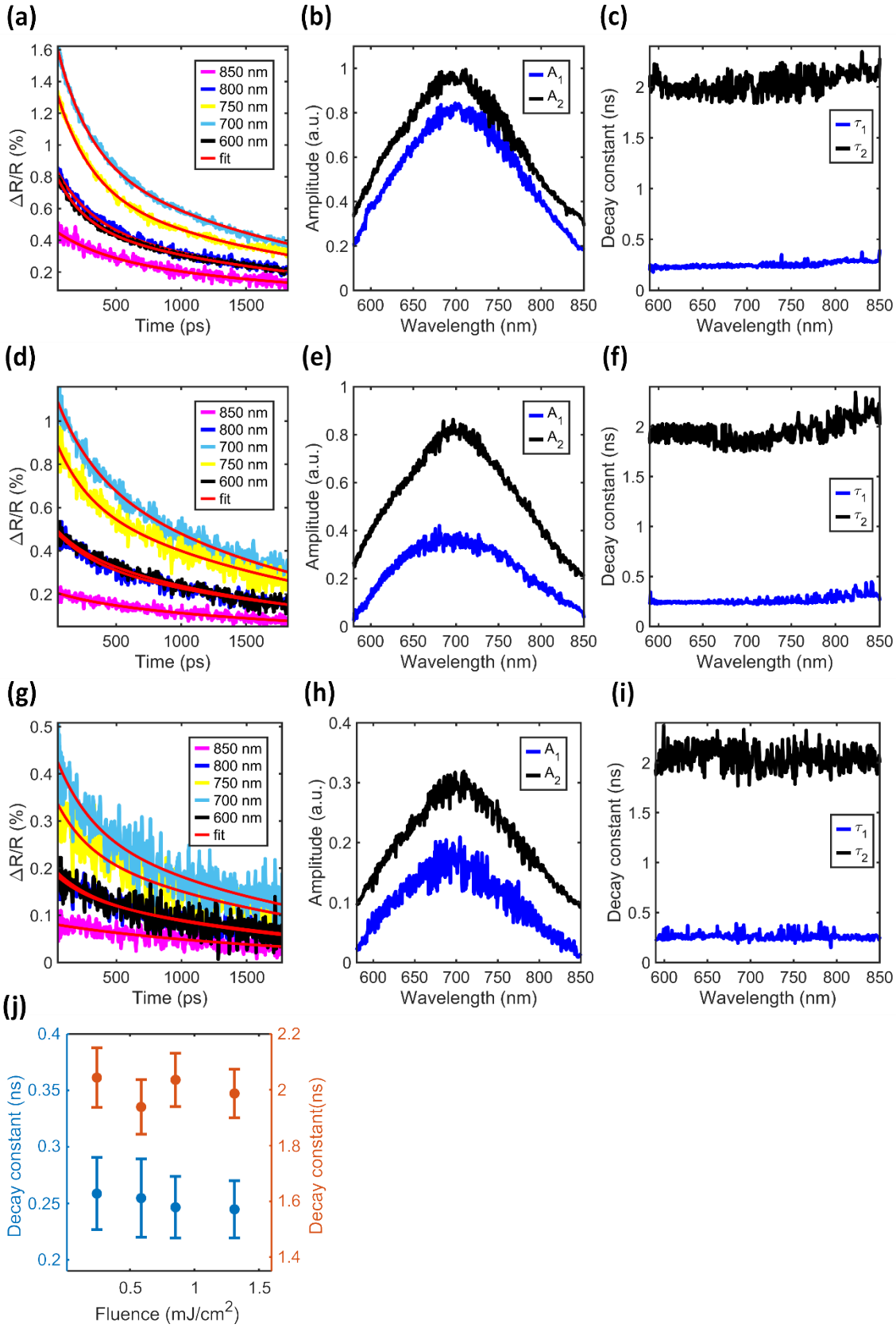

Fig. S12 Single-wavelength fitting results of the longer-time dynamics using a biexponential function for three pump fluences. Panels (a–c), (d–f), and (g–i) correspond to pump fluences of 0.85, 0.59, and 0.24 mJ/cm^2, respectively. In each set, the panels show selected DR time traces and corresponding fit curves, amplitude parameter dependence on probe wavelength, and decay constant parameter dependence on probe wavelength. (j) Average decay constants as a function of pump fluence.

References

S1 M. A. ElGhazali, P. G. Naumov, Q. Mu, V. Süß, A. O. Baskakov, C. Felser and S. A. Medvedev, Pressure-induced metallization, transition to the pyrite-type structure, and superconductivity in palladium disulfide PdS_2, *Phys. Rev. B*, 2019, **100**, 014507, DOI: 10.1103/PhysRevB.100.014507.

S2 R. Kempt, A. Kuc and T. Heine, Two-dimensional noble-metal chalcogenides and phosphochalcogenides, *Angew. Chem. Int. Ed.*, 2020, 59, 9242–9254.

S3 M. Ghorbani-Asl, A. Kuc, P. Miró and T. Heine, A single-material logical junction based on 2D crystal PdS_2, *Adv. Mater*., 2016, **28**, 853–856.

S4 P. A. Temple and C. E. Hathaway, Multiphonon Raman spectrum of silicon, *Phys. Rev. B*, 1973, **7**, 3685–3697.

S5 C. S. Wang, J. M. Chen, R. Becker and A. Zdetsis, Second-order Raman spectrum and phonon density of states of silicon, *Phys. Lett. A*, 1973, **44**, 517–518.

S6 W.-J. Lee and Y.-H. Chang, Growth without postannealing of monoclinic VO_2 thin film by atomic layer deposition using VCl_4 as precursor, *Coatings*, 2018, **8**, 431, DOI: 10.3390/coatings8120431.

S7 P. Borowicz, M. Latek, W. Rzodkiewicz, A. Łaszcz, A. Czerwiński and J. Ratajczak, Deep-ultraviolet Raman investigation of silicon oxide: thin film on silicon substrate versus bulk material, *Adv. Nat. Sci.: Nanosci. Nanotechnol.,* 2012, **3**, 045003, DOI: 10.1088/2043-6262/3/4/045003.

S8 V. Kidalov, S. Kukushkin, A. Osipov, A. Redkov, A. Grashchenko, I. Soshnikov, M. Boiko, M. Sharkov and A. Dyadenchuk, Properties of SiC films obtained by the method of substitution of atoms on porous silicon, *ECS J. Solid State Sci. Technol.*, 2018, **7**, P158–P160.

S9 P. Borowicz, A. Taube, W. Rzodkiewicz, M. Latek and S. Gierałtowska, Raman spectra of high-κ dielectric layers investigated with micro-Raman spectroscopy: comparison with silicon dioxide, *Sci. World J*., 2013, **2013**, 208081, DOI: 10.1155/2013/208081.

S10 X. Zhang, G. Su, J. Lu, W. Yang, W. Zhuang, K. Han, X. Wang, Y. Wan, X. Yu and P. Yang, Centimeter-scale few-layer PdS_2: fabrication and physical properties, *ACS Appl. Mater*. Interfaces, 2021, **13**, 43063–43074.

S11 H. Gao, H. Y. Zhou, Y. L. Hao, G. L. Zhou, H. Zhou, F. L. Gao, J. B. Xiao, P. H. Tang and G. L. Hao, Controllable growth of wafer-scale PdS and PdS_2 nanofilms via chemical vapor deposition combined with an electron beam evaporation technique, *J. Semicond*., 2023, **44**, 122001, DOI: 10.1088/1674-4926/44/12/122001.

S12 K. He, W. Xu, J. Tang, Y. Lu, C. Yi, H. Zhu, H. Zhang, X. Lin, Y. Feng, M. Zhu, J. Shen, M. Zhong and X. Duan, Centimeter-scale PdS_2 ultrathin films with high mobility and broadband photoresponse, *Small*, 2023, **19**, e2206915, DOI: 10.1002/smll.202206915.

S13 H. S. Jo, G. H. Oh, S. Kim et al., Atomically thin PdS_2: physical characteristics and electronic device applications, *J. Korean Phys. Soc*., 2023, **83**, 751–755.

S14 C. C. Katsidis and D. I. Siapkas, General transfer-matrix method for optical multilayer systems with coherent, partially coherent, and incoherent interference, *Appl. Opt*., 2002, **41**, 3978–3987.

S15 K. Chen, R. Ghosh, X. Meng et al., Experimental evidence of exciton capture by mid-gap defects in CVD-grown monolayer $MoSe_2$, *npj 2D Mater. Appl.*, 2017, **1**, 15, DOI: 10.1038/s41699-017-0019-1.